

Evaluation of WRF Modeling in Relation to Different Land Surface Schemes and Initial and Boundary Conditions

A Snow Event Simulation Over the Tibetan Plateau

Liu, Lian; Ma, Yaoming; Menenti, Massimo; Zhang, Xinzhong; Ma, Weiqiang

DOI

[10.1029/2018JD029208](https://doi.org/10.1029/2018JD029208)

Publication date

2019

Document Version

Final published version

Published in

Journal of Geophysical Research: Atmospheres

Citation (APA)

Liu, L., Ma, Y., Menenti, M., Zhang, X., & Ma, W. (2019). Evaluation of WRF Modeling in Relation to Different Land Surface Schemes and Initial and Boundary Conditions: A Snow Event Simulation Over the Tibetan Plateau. *Journal of Geophysical Research: Atmospheres*, 124(1), 209-226.
<https://doi.org/10.1029/2018JD029208>

Important note

To cite this publication, please use the final published version (if applicable).
Please check the document version above.

Copyright

Other than for strictly personal use, it is not permitted to download, forward or distribute the text or part of it, without the consent of the author(s) and/or copyright holder(s), unless the work is under an open content license such as Creative Commons.

Takedown policy

Please contact us and provide details if you believe this document breaches copyrights.
We will remove access to the work immediately and investigate your claim.

JGR Atmospheres

RESEARCH ARTICLE

10.1029/2018JD029208

Key Points:

- Land surface schemes (CLM, Noah, and Noah-MP) and atmospheric forcing (NCEP-FNL and ERA-Interim) were applied in WRF to analyze a snow event
- We found that sensitivity of air temperature to land surface schemes is larger than to the forcing with best performance WRF + CLM
- We found that simulations of solid precipitation are more accurate when applying CLM or Noah-MP + ERA-Interim in WRF

Supporting Information:

- Supporting Information S1
- Figure S1

Correspondence to:

L. Liu and Y. Ma,
lliu@itpcas.ac.cn;
ymma@itpcas.ac.cn

Citation:

Liu, L., Ma, Y., Menenti, M., Zhang, X., & Ma, W. (2019). Evaluation of WRF modeling in relation to different land surface schemes and initial and boundary conditions: A snow event simulation over the Tibetan Plateau. *Journal of Geophysical Research: Atmospheres*, 124, 209–226. <https://doi.org/10.1029/2018JD029208>

Received 20 JUN 2018

Accepted 15 DEC 2018

Accepted article online 22 DEC 2018

Published online 15 JAN 2019

Evaluation of WRF Modeling in Relation to Different Land Surface Schemes and Initial and Boundary Conditions: A Snow Event Simulation Over the Tibetan Plateau

Lian Liu^{1,2} , Yaoming Ma^{1,3,2} , Massimo Menenti^{4,5}, Xinzhong Zhang⁶, and Weiqiang Ma^{1,3}

¹Key Laboratory of Tibetan Environment Changes and Land Surface Processes, Institute of Tibetan Plateau Research, Chinese Academy of Sciences, Beijing, China, ²University of Chinese Academy of Sciences, Beijing, China, ³CAS Center for Excellence in Tibetan Plateau Earth Sciences, Beijing, China, ⁴State Key Laboratory of Remote Sensing Science, Institute of Remote Sensing and Digital Earth, Chinese Academy of Sciences, Beijing, China, ⁵Delft University of Technology, Delft, Netherlands, ⁶Beijing Presky Technology Co., Ltd, Beijing, China

Abstract Snowfall and the subsequent evolution of the snowpack play important roles in the cryospheric and hydrospheric processes that occur on the Tibetan Plateau (TP). Current literature provides scarce evidence covering the sensitivity of solid precipitation to land surface physics schemes and initial and boundary conditions on the TP. Six numerical experiments using the Weather Research and Forecasting (WRF) model were conducted to simulate a snow event over the TP in March 2017. Different land surface physics schemes, that is, Community Land Model (CLM), Noah, and Noah-MP, and initial and boundary conditions provided by atmospheric reanalysis data sets, that is, the National Centers for Environmental Prediction-FNL and ERA-Interim data sets, were applied in sensitivity analyses. The observed near-surface air temperature, snow depth, and snow water equivalent (SWE) values were used to evaluate each model's performance. The results demonstrate that (1) the sensitivity of the near-surface air temperature to land surface physics schemes is greater than it is to both the initial and boundary conditions; (2) the best performance is achieved when applying WRF + CLM with a root-mean-square error of 8.4 °C, a mean absolute deviation of 7.3 °C, a correlation coefficient of 0.75, and a spatial correlation coefficient of ~0.5 to air temperature estimates. A potentially important factor appears to be the advanced parametrization of albedo in the CLM scheme; (3) the advanced land surface schemes in the WRF model describes the physics of cryospheric and hydrospheric processes in detail, and the land surface response is determined by multiple variables and parameters in such schemes. The spatial patterns in such variables and parameters determined the detailed spatial variabilities observed in snow cover and amount and its temporal evolution. The WRF model overestimates, however, the intensity and extent of snow depth and SWE; (4) simulations of solid precipitation are more accurate when applying CLM or Noah-MP + ERA-Interim in WRF; and (5) WRF performance with regard to SWE estimates clearly depends upon the discrimination of lighter from heavier snowfall.

1. Introduction

The Tibetan Plateau (TP) is known as the Third Pole (Qiu, 2008). It has a mean altitude exceeding 4,000 m above sea level and is characterized by strong land-atmosphere interactions (Ma et al., 2008; Zhang et al., 2008). Land surface physics plays a significant part in determining the global water vapor and energy budget at the land-atmosphere interface, which in turn affects the nature of atmospheric circulation and even causes climate feedbacks in the long term (Roesch et al., 2001). Atmospheric dynamic and thermodynamic processes can present different observable features at the land surface.

Regional climate models use a relatively high spatial resolution and can accurately simulate regional and local weather patterns, which are greatly affected by the complexities of the underlying surface (Gao et al., 2002). The Weather Research and Forecasting (WRF) Model is a state-of-the-art mesoscale numerical weather prediction system designed for both atmospheric research and operational forecasting applications (Skamarock et al., 2008). It is a fully compressible and nonhydrostatic model that employs a terrain-following mass vertical coordinate and Arakawa C-grid and uses Runge-Kutta second- and third-order integration in time and a second- to sixth-order integration in its advection scheme. The WRF model allows for

the application and evaluation of several alternative parametrization schemes addressing both boundary layers and land surface processes and feeds into a wide range of meteorological applications across scales from tens of meters to thousands of kilometers (Chen & Dudhia, 2001; Niu et al., 2011; Pleim & Xiu, 1995; Smirnova et al., 2000; Xue et al., 1991). The WRF model can be accurately applied to the TP's complex terrain, and is able to provide meteorological variables at high resolution to compensate for any uneven distribution and scarcity of in situ meteorological observations (Gao et al., 2015; Li et al., 2009; Ma & Ma, 2016; Maussion et al., 2011; Sato et al., 2008).

Accuracy of initial and boundary conditions is crucial to the successful production of WRF simulations. There is some evidence that basic meteorological factors (e.g., temperature and specific humidity) derived from European Centre for Medium-Range Weather Forecasts (ECMWF) reanalysis data sets differ from those extracted from National Centers for Environmental Prediction (NCEP) data sets (Grotjahn, 2008; Renwick, 2004). Some simulations have used initial and boundary conditions generated from ECMWF reanalysis data sets (ERA-Interim; Collier et al., 2013; Kryza et al., 2017; Soares et al., 2012), and others have employed initial and boundary conditions generated from NCEP final analysis data sets (NCEP-FNL; Li et al., 2009; Ma & Ma, 2016; Maussion et al., 2011). Precipitation values have appeared well reproduced when NCEP-FNL data have been used (Maussion et al., 2014), while initialization values using ERA-Interim data have rendered reasonable results for snow cover simulations over the TP (Collier et al., 2013).

Various land surface schemes have been implemented in the more recent versions of the WRF model. In WRF version 3.1, soil moisture and temperature values across four layers, snowpack depth and SWE values across a single snow layer, and the canopy water content, energy budget, and water flux values are all simulated using the Noah land surface model (LSM; Chen & Dudhia, 2001). The multiphysics Noah LSM (Noah-MP) model has also been coupled with WRF version 3.4 (Niu et al., 2011; Yang et al., 2011). The Noah-MP model contains independent vegetation canopy and bare ground parameters, a separate glacier modeling program, and a complex multilayer snowpack physics modeling program across a maximal three layers. Various options are available for vegetation schemes, canopy stomatal resistance, and radiation transfer in Noah-MP. The Community Land Model (CLM) has been coupled with WRF version 3.5 to produce complex parametrizations of dynamic vegetation patterns, hydrological characteristics and surface energy balance (Lawrence & Chase, 2010). CLM includes a single canopy layer, up to 5 snowpack layers and 10 soil layers, providing more advanced estimations of soil hydrology and snow processes. Jin et al. (2010) pointed out that land surface physics enormously influences temperature simulations. The use of the WRF + CLM model would therefore improve near-surface temperature simulations.

Snow plays an important role in both the energy budget and the water cycle with its large variations in surface albedo, thus net radiation, snow water storage, and its meltwater release (Liu & Qian, 2005). We took there to be two different snow event stages, which determine the surface mass balance of glaciers, that is, snowfall and subsequent snowmelt. These processes occur widely over the TP, especially at high altitudes. Large variations in albedo values can occur during a snow event. Snow responds rapidly to any change in the climate. Much research has therefore been conducted into snow cover, snow depth (SD), and snow water equivalent (SWE) values on the TP (Li et al., 2009; Liu & Chen, 2011; Maussion et al., 2011; Qin et al., 2006; Xie et al., 2018; Zhao et al., 2007). Zhu and Dong (2013) pointed out that phase five of the Coupled Model Intercomparison Project (CMIP5) models can overestimate mean spring snow cover over the TP's complex topography. Wei and Dong (2015) assessed SD achieved by CMIP5 models and pointed out that maximum snow regions were well modeled by most models, but the maximum SD values were overestimated by 5–15 times that of the observed. SWE values simulated by the Regional Climate Model version 4.0 (RegCM4; Giorgi et al., 2012) and nested in the global climate model BCC_CSM (<http://forecast.bccsm.ncc-cma.net/htm/>) were lower than measurements made using passive microwave and ground observations by 0.1–10 mm in most regions of the TP (Ji & Kang, 2013). Not all the above mentioned models have the ability to obtain the spatial distributions of snow variables. Problems remain with the SD and SWE values simulated by LSMs or global climate models (Toure et al., 2016; Xia et al., 2014).

Snow falls frequently on the TP, especially at high altitudes. Snowfall and the subsequent evolution of the snowpack therefore play a vital role in determining the cryospheric and hydrospheric processes, which occur on the TP. The melting and refreezing of snow determine the mass balances of the region's glaciers. Radiative forcing at the land-atmosphere interface strongly relies on land surface albedo, which is highly

Table 1
Parameters Used in the Numerical Experiments

Simulations time period	5–15 March 2017
Nest	False
Projection	Mercator
Center of domain	84.95°E, 23.18°N
Resolution	25 km
Grid points in <i>x</i> and <i>y</i> coordinate system	260 × 180
Layers in vertical	30
Microphysics	Lin scheme
Longwave radiation	RRTM scheme
Shortwave radiation	Dudhia scheme
Surface layer	Revised MM5 Monin-Obukhov scheme
Planetary boundary layer	YSU scheme
Cumulus parameterization	Kain-Fritsch scheme

variable and depends on both SD values and the age of any lying snow. Modeling snowfall events and the evolution of the snowpack, therefore, requires the use of coupled atmosphere-LSMs; the WRF model is a good candidate for this purpose because it has the capacity to simulate and predict snow events (Kalinin et al., 2015; Yu, 2013). It can thus be regarded as meaningful to simulate snow events using coupled atmosphere-LSMs like the WRF model. Literature offers scarce evidence on the sensitivity of the WRF modeling of solid precipitation and SWE values within LSMs and initial and boundary conditions, especially in a complex terrain like the TP. More work is therefore required to establish which initial and boundary conditions, and which specific LSM scheme, perform better over the whole TP. This study addresses such a comparative evaluation. We designed and conducted six numerical experiments using WRF modeling to simulate a severe snowstorm (and the subsequent evolution of the snowpack), which occurred over a sizeable proportion of the TP from 5 to 15 March 2017, applying two atmospheric analyses data sets (i.e.,

NCEP-FNL and ERA-Interim) and three LSMs (i.e., Noah, Noah-MP, and CLM) to the experimentation. This work aims at acquiring the optimal initial and boundary conditions, and LSM configuration, required to simulate a severe snow event over the TP. Our experimentation will form the basis of our follow-up work and presents a possible approach, which can be employed when using WRF modeling to study snow events on the TP.

2. Data and Methodology

2.1. Selection of the Snow Event

Spring snow anomalies over the TP can be associated with summer monsoonal rainfall in East Asia (Xiao & Duan, 2016). Blanford (1884) was the first to point out that the pattern of winter-spring snowfall in the Himalaya Mountains exhibited a negative correlation with the succeeding summer's monsoonal rainfall. Detailed investigations have elucidated that the interdecadal increase in spring SD values on the TP can be associated with wetter (drier) summer rainfall in the Yangtze River Valley (in the southeastern coast of China; Zhang et al., 2004). It is therefore meaningful to investigate spring snow processes on the TP. A severe snow event occurred over a large proportion of the TP from 5 to 15 March 2017. The heaviest snowfall took place on 11 March in Nielamu County, on the border between China and Nepal, where total SWE was 89.2 mm and SD reached 61 cm (http://politics.gmw.cn/2017-03/11/content_23944835.htm). During this event the wind force reached 10 on the Beaufort scale, and the air temperature observed at the adjacent Pagri Meteorological Station decreased rapidly by 6 K.

2.2. Model Configuration and Experimental Designs

Snowfall and the subsequent evolution of the snowpack are important contributors to the energy budget since they directly control albedo values. Radiative forcing at the land-atmosphere interface is determined by these albedo values, which in turn depend on SD values and the age of any lying snow. As a coupled atmosphere-LSM, the WRF model simulates snow events well. This is because the WRF model can incorporate various reanalysis data sets when inputted and use this information to form its initial and boundary condition parameters; the NCEP-FNL (Kalnay et al., 1996) and ERA-Interim (Berrisford et al., 2009) reanalysis data sets are those most frequently used for this purpose. The NCEP-FNL operational global analysis product is derived from the Global Data Assimilation System. We used a 0.25° by 0.25° horizontal resolution with a 6-hourly interval, taken from <https://rda.ucar.edu/datasets/ds083.3/>. The ERA-Interim atmospheric reanalysis data set is produced by a data assimilation system based on the Integrated Forecast System used by the ECMWF and covers a data-rich period, while continuing to update in real time. Berrisford et al. (2009) detailed the ERA-Interim product archive, describing its atmospheric forecast model and sequential data

Table 2
Experimental Designs

Experiments	CLM	Noah	Noah-MP
ERA-Interim	EXP1	EXP3	EXP5
NCEP-FNL	EXP2	EXP4	EXP6

Note. CLM = Community Land Model.

Table 3
Options Applicable to the Noah-MP LSM

Parameters in Noah-MP	Parameterization schemes
Canopy stomatal resistance	Ball-Berry scheme
Soil moisture factor for stomatal resistance	Noah scheme
Runoff and groundwater	TOPMODEL with groundwater
Surface layer drag coefficient	Monin-Obukhov
Soil permeability option	Linear effect, more permeable
Radiation transfer	Two-stream applied to vegetated fraction
Ground surface albedo option	CLASS (Canadian Land Surface Scheme)
Snow/soil temperature time scheme	Semi-implicit

assimilation schemes, as well as the performance of such systems (Dee et al., 2011). We used a 0.25° by 0.25° horizontal resolution with a six hourly interval, taken from <http://apps.ecmwf.int/datasets/data/interim-full-daily/>.

Land-atmosphere coupling is significant with regard to the processes of snowfall and the subsequent evolution of the snowpack (Ikeda et al., 2010). We determined the quantities of solid precipitation using both microphysics and LSMs, as applied in WRF. The quantities of water in different states were calculated using the Lin microphysics scheme, that is, water vapor, cloud water, cloud ice, rain, snow, and hail (Lin et al., 1983). In the microphysics schemes we employed, the process of snow formation includes the conversion of cloud ice to snow, and the collision and coalescence growth of snow crystals. The transformation of cloud ice to snow was simulated using the aggregation and Bergeron processes, which

delineated the basic mechanisms of snow formation. Sublimation and snowmelt were also taken into consideration when estimating the reduction in snow content using LSMs. The simulation of solid precipitation depends upon a combination of the meteorological conditions and LSMs.

This snow event was numerically simulated using the parameter settings detailed in Table 1. To evaluate the capability of the three selected LSMs to describe the snow event, we conducted six numerical experiments using WRF version 3.7.1 by combining both the NCEP-FNL and ERA-Interim data sets with various LSMs, that is, Noah, Noah-MP, and CLM (Table 2). The options selected when applying the Noah-MP LSM are detailed in Table 3.

The Noah-MP LSM includes more advanced physical parametrization schemes and is more complex than the simpler Noah LSM. The Noah LSM uses a surface layer, which combines vegetation with a bulk layer

of snow and soil. The percolation and refreezing of snow meltwater are not possible to discern in such a bulk snow layer structure. Other shortcomings of the Noah LSM is that frozen soil is impervious. In addition to the baseline Noah LSM, the Noah-MP LSM uses a separate vegetation canopy layer and three snow layers. In the Noah-MP LSM, a modified two-stream radiation transfer scheme which takes a vegetation gap into account is used to calculate the absorbed irradiance by sunlit and shaded leaves, separately, while longwave radiation and heat fluxes are calculated over vegetated and bare ground areas. The Noah-MP LSM also models up to three layers of snow and includes the processes of percolation and the refreezing of snow meltwater; further, it takes into account the potential presence of a permeable frozen soil fraction. Any snow accumulation estimate is sensitive to the partitioning of precipitation into rain and snow. Whereas the Noah-MP LSM applies a relatively complex functional form to such a partitioning, the Noah LSM simply assumes snowfall to have occurred when the surface air temperature is lower than the freezing point, and vice versa for rainfall. The detailed differences between the Noah and Noah-MP LSMs have been described in previously-published documentation (e.g., Cai et al., 2014; Chen, Barlage, et al., 2014; Chen, Liu, et al., 2014; Niu et al., 2011).

Yu (2013) conducted numerical experiments applying alternate land surface physics and microphysics schemes to a snow event. The best performance was obtained with the Noah LSM and Lin schemes. In our six numerical experiments, the selection of microphysics and cumulus parametrization schemes was based on Yu's overall simulation results. The model's domain, the topography as mapped by 3 arc sec Shuttle Radar Topography Mission data, and the distribution of surface meteorological stations are shown in Figure 1. The model's domain ranges from the

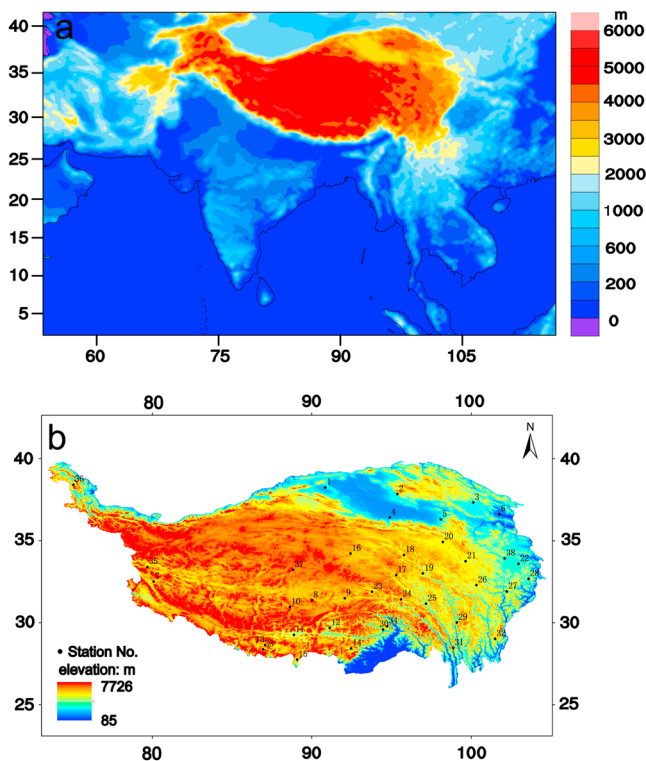


Figure 1. Weather Research and Forecasting domain and topography (a); and a 3-arc sec Shuttle Radar Topography Mission, with the distribution of the in situ meteorological stations listed in Table 4 (b).

Table 4

In situ CMA and CAS stations (the Modeled Altitude Minus the Actual Altitude of In Situ Stations is Expressed as the Altitudinal Difference; Aspects Were Obtained From a High-Resolution SRTM Data Set)

Station type	Station no.	Name	ID	Latitude (°N)	Longitude (°E)	Elevation (m)	Altitudinal difference (m)	Aspect (degree)
CMA	1	Mangnai	51886	38.25	90.85	2,945.0	0.8	245.0
	2	Daqaidam	52713	37.85	95.37	3,174.0	31.8	268.2
	3	Gangca	52754	37.33	100.13	3,302.0	54.9	225.0
	4	Golmud	52818	36.42	94.90	2,807.6	-7.8	324.5
	5	Doulan	52836	36.30	98.10	3,189.0	5.7	18.4
	6	Xining	52866	36.62	101.77	2,295.2	41.8	339.0
	7	Shiquanhe	55228	32.50	80.08	4,278.6	27.9	138.7
	8	Baingoïn	55279	31.37	90.02	4,700.0	217.1	90.0
	9	Nagqu	55299	31.48	92.07	4,507.0	54.0	5.2
	10	Xainza	55472	30.95	88.63	4,672.0	95.9	69.0
	11	Xigaze	55578	29.25	88.88	3,836.0	57.6	355.7
	12	Lhasa	55591	29.67	91.13	3,648.9	143.9	135.0
	13	Tingri	55664	28.63	87.08	4,300.0	119.8	343.5
	14	Lhunze	55696	28.42	92.47	3,860.0	509.0	223.3
	15	Pagri	55773	27.73	89.08	4,300.0	164.7	133.0
	16	Tuotuohe	56004	34.22	92.43	4,533.1	13.4	180.0
	17	Zadoi	56018	32.90	95.30	4,066.4	304.7	205.2
	18	Qumarleb	56021	34.13	95.78	4,175.0	89.2	242.1
	19	Yushu	56029	33.00	96.97	3,716.9	423.8	0.0
	20	Madoi	56033	34.92	98.22	4,272.3	64.9	225.0
	21	Darlag	56046	33.75	99.65	3,967.5	161.6	45.0
	22	Ruoergai	56079	33.58	102.97	3,441.4	38.3	136.5
	23	Sogxian	56106	31.88	93.78	4,024.0	307.5	55.7
	24	Dengqen	56116	31.42	95.60	3,873.1	268.2	130.9
	25	Qamdo	56137	31.15	97.17	3,315.0	308.7	185.5
	26	Sertar	56152	32.28	100.33	3,894.0	158.3	270.0
	27	Barkam	56172	31.90	102.23	2,664.4	648.1	211.4
	28	Songpan	56182	32.67	103.60	2,850.7	971.2	89.0
	29	Batang	56247	30.00	99.10	2,589.2	501.9	296.6
	30	Nyingchi	56312	29.57	94.47	2,991.8	415.9	163.3
	31	Deqen	56444	28.45	98.88	3,319.0	-50.2	115.8
	32	Jiulong	56462	29.00	101.50	2,925.0	700.8	54.3
CAS	33	QOMS		28.21	86.56	4,276.0	341.0	353.7
	34	SETS		29.77	94.73	3,326.0	558.1	91.9
	35	NASDE		33.39	79.70	4,264.0	165.2	59.0
	36	MASWE		38.41	75.05	3,668.0	113.2	8.1
	37	SHSEX		33.22	88.83	4,947.0	28.1	194.0
	38	MAQU		33.92	102.10	3,440.0	-6.1	246.8

Note. Qomolangma station (QOMS), Southeast Tibet station (SETS), Ngari station (NASDE), Muztagh Ata station (MASWE), ShuangHu station (SHSEX), and MAQU station (MAQU). SRTM = Shuttle Radar Topography Mission; CAS = Chinese Academy of Sciences; CMA = China Meteorological Administration.

Tianshan Mountains to the southern Indian Peninsula, and from central Iran to eastern China. Such a domain allows to capture the westerlies, the Indian monsoonal atmospheric circulations and any land-ocean interactions which may exert a potentially significant effect on the TP.

2.3. Evaluation of the Model's Performance

To assess the WRF model's performance, we compared field observations of near-surface air temperatures, albedo values, and SD and SWE measurements with the model's estimated values. Near-surface air temperature is determined by land-atmosphere interactions and controls precipitation (liquid or solid) and the rate of snowmelt. Thus, we first examined near-surface air temperatures recorded by 32 World Meteorological Organization surface synoptic observation (SYNOP) stations run by the China Meteorological Administration (CMA) to evaluate the model's performance. Albedo values were observed at six Chinese Academy of Sciences (CAS) stations and captured the two snowfall and snowmelt stages (Figure 1 and Table 4). The albedo appears to increase rapidly with snowfall and decrease gradually with the

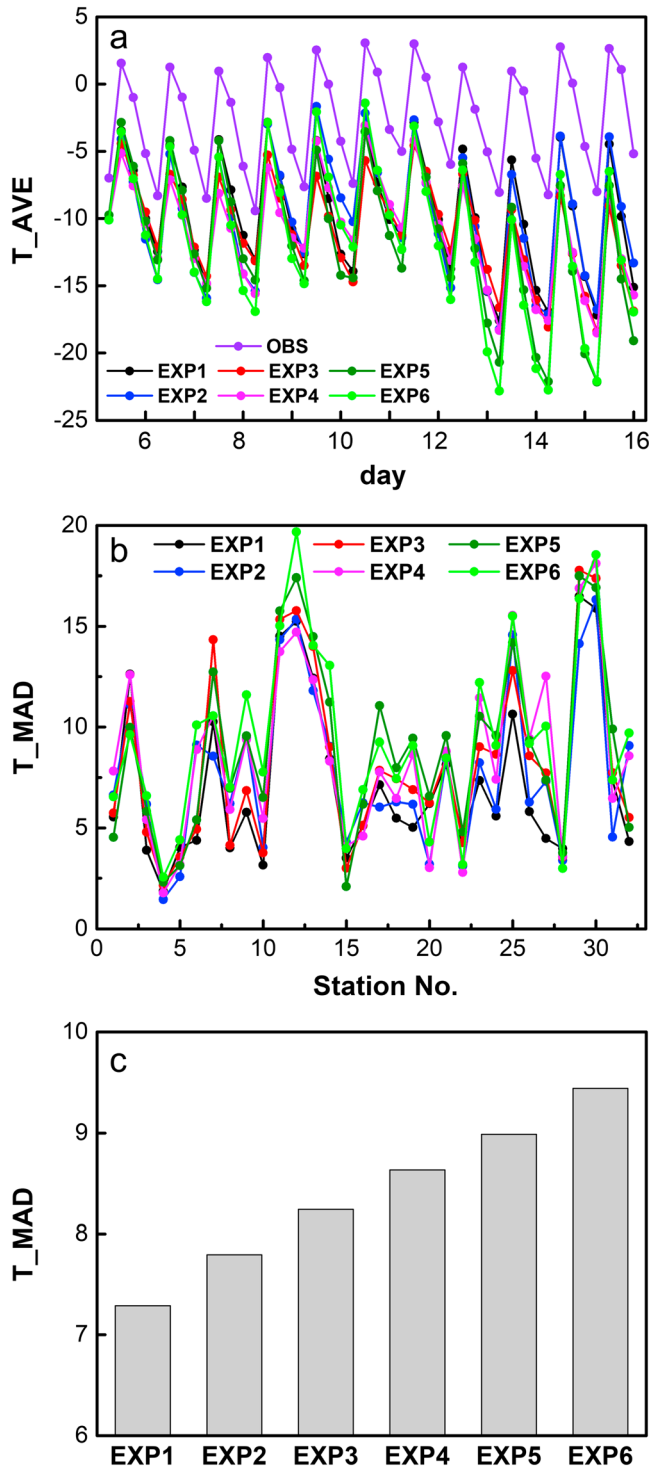


Figure 2. Time series of mean near-surface air temperatures from the meteorological stations listed in Table 4 for observed in situ measurements (purple lines) and the six simulated numerical experiments (X axis shows days in March; a); MAD of near-surface air temperatures from each meteorological station (X axis shows station nos., as listed in Table 4; b); and a 32 station mean for the six numerical experiments (c). For a description of the experiments, see Table 2.

subsequent snowmelt, dependent upon SD and snow age. The root-mean-square error (RMSE), mean absolute deviation (MAD), correlation coefficient (CC), and spatial CC (SCC) were used to evaluate the model's performance.

A static topography as produced by the U.S. Geological Survey in 1996 using a 2-arc min resolution was used in the WRF model to cover the whole of the topographically complex TP. To document how in situ observations are affected by the complex terrain, 1° windows surrounding some of the in situ meteorological stations are shown in Figure S1 in the supporting information. As seen in Table 4, the topographic altitudinal difference between the model and the real altitudes has been recorded (Figure 1 and Table 4). This caused a bias in near-surface air temperature estimates, which was corrected by adjusting the temperature to the correct altitude by applying the lapse rate. The latter ranges from a constant 6 °C/km (Dodson & Marks, 1997) to 6.5 °C/km (Gerlitz et al., 2014; Stahl et al., 2006). The actual lapse rate in a given region might also have been applied, but it is a rather complex variable and requires dense and accurate in situ surface observations, of which there are too few from the TP (Gao et al., 2017). Accordingly, we estimated the lapse rate on the basis of literature and used a specific March lapse rate of 7.1 °C/km (Kunkel, 1989; Liston & Elder, 2006).

3. Results

3.1. Near-Surface Air Temperatures

The time series of 6-hourly near-surface air temperature estimates from the six numerical experiments were compared with observations from CMA stations (Figure 2a). The WRF model's performance appears to differ between different stations, dependent upon their location (Figure 2b). For example, the MAD values between observed and simulated near-surface air temperatures are ~2 °C for the Golmud meteorological station but are greater than 14 °C for the Lhasa, Batang, and Nyingchi meteorological stations. These near-surface air temperature MAD values are averaged over these meteorological stations for each individual experiment and are shown in Figure 2c. The lowest MAD value is 7.3 °C when CLM and ERA-Interim data are applied; the largest MAD value is 9.4 °C when applying Noah-MP LSM and NCEP-FNL data. Near-surface air temperature MAD values are always 0.4 °C higher for experiments that use NCEP-FNL data than those which employ ERA-Interim data, and the same LSM. In addition to differences in altitude between the model's grid and the meteorological stations, the smoothing of the terrain due to the topographical model applied in WRF appears to have another consequence. The smoother WRF topography filters out terrain-related local circulations and radiative fluxes, causing the inaccuracies in modeled near-surface air temperatures. An additional factor is the mismatch in land surface type between the one applied in the LSMs and the actual one at the locations of any of the stations. Land surface type essentially affects radiation flux values and near-surface air temperatures (Russell & Cai, 2004). We used 24-class land cover data sets with a 2-arc min resolution produced by the U.S. Geological Survey between 1992 and 1993 in all our experiments. Such old land cover data sets may not represent the actual situations at, or around, the meteorological stations. For

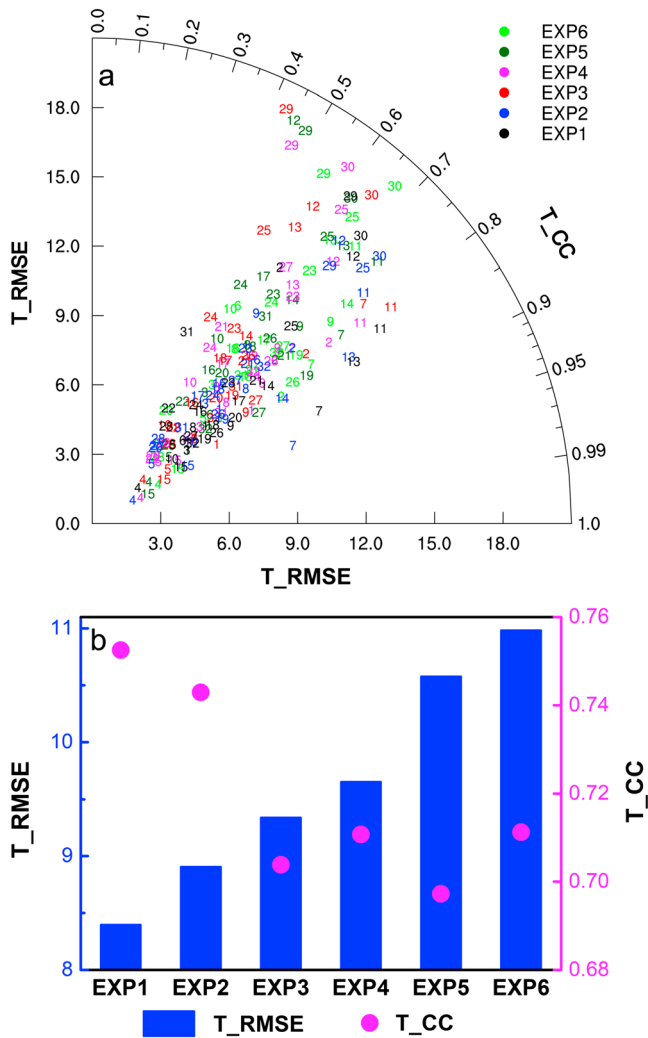


Figure 3. Root-mean-square error (RMSE) and correlation coefficient (CC) values for near-surface air temperatures for each meteorological station, with the station no. correlative with the stations listed in Table 4 (X axis shows RMSE of near-surface air temperatures; a); and a 32 station mean for the six experiments (b). For a description of the experiments, see Table 2.

example, the model assumes that the land cover at QOMS is composed of grassland and is of a mixed grassland variety at NASDE, whereas both sites are in reality either barren or sparsely vegetated.

The observed and simulated RMSE and CC values of near-surface air temperatures were then calculated, and any differences noted (Figure 3). The CC values are concentrated between 0.6 and 0.8 for most stations, while RMSE values are more scattered (Figure 3a). It is difficult to achieve a reliable model performance at some meteorological stations due to their geographical location and complex surrounding terrain. The best performance is achieved when the CLM protocol is used (in EXP1 and EXP2), similarly to the results reported by Jin et al. (2010), with RMSE = 8.4 °C and CC = 0.75 in EXP1 and RMSE = 8.9 °C and CC = 0.74 in EXP2 in this study (Figure 3b).

In order to investigate the spatial distribution of near-surface air temperatures, we interpolated the few available observations using the Cressman interpolation method to obtain a regionalized observation field, before repeating the comparison with the modeled results (Figure 4). The SCC was used to evaluate the accordance of simulated spatial pattern of model temperature with reality (Figure 4h and Table 5). Modeled temperatures are colder than observed temperatures on the central TP, and warmer on the southeastern TP, with modeled results from all experiments giving similar spatial patterns (Figures 4a–4g). SCC values change with time from a weak correlation before snowfall to a slightly higher correlation after snowfall. Overall, all experiments exhibit similar spatial patterns and SCC values less than 0.5; EXP1 and EXP2 display slightly higher correlations with observed air temperatures.

3.2. Albedo

The albedo determines surface net shortwave radiation and depends on SD and snow age. It changes rapidly and significantly during periods of snowfall and any subsequent snowmelt. It is determined as the ratio of reflected shortwave radiation (up) to shortwave irradiance (down). At the local solar noon in Lhasa (i.e., 14:00 Beijing Standard Time (BST)), the observed albedo value is closer to the Lambertian albedo described by the WRF LSMs. We therefore chose the observed albedo at 14:00 BST to evaluate the model's albedo. The time series of the observed albedo measurements recorded at 14:00 BST is displayed in

Figure 5a and shows that snowfall did not occur at NASDE and SETS but that it did occur at QOMS, MASWE, MAQU, and SHSEX.

Albedo is influenced by various factors like SD, the solar zenith angle and soot deposition. It is difficult to obtain accurate estimates of albedo values using the model. The albedo parametrization scheme within the Noah LSM considers snow cover, snow age, snow albedo and fractional vegetation. In addition, the Noah-MP LSM incorporates soil water content. In the CLM protocol, additional factors are taken into account, such as effective ice grain size. Comparing observed albedo measurements with modeled estimates (Figure 5b), the lowest RMSE of 0.24 and the highest CC value of 0.36 are obtained when using CLM and NCEP-FNL data sets (for EXP2). The albedo RMSE is the lowest when applying CLM (for EXP1 and EXP2) to the model. The highest albedo RMSE is obtained when applying Noah LSM (EXP3 and EXP4). Though the CC value is low in every experiment, a slightly better correlation is achieved when using NCEP-FNL data (i.e., for EXP2, EXP4, and EXP6) than ERA-Interim data (for EXP1, EXP3, and EXP5). Even better results are obtained when applying CLM with NCEP-FNL, due to the application of multiple snow surface properties to the parametrization of albedo values. The worst

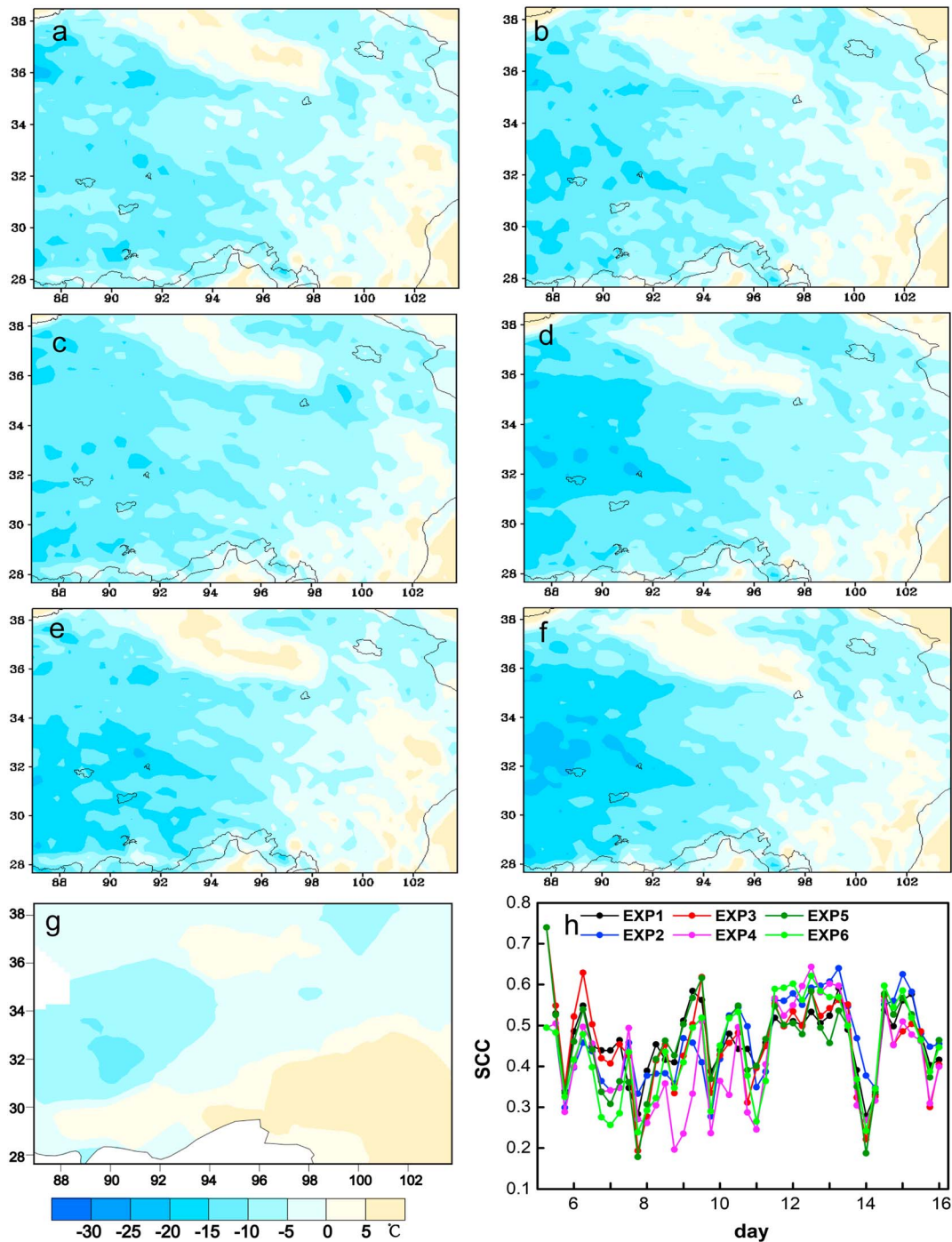


Figure 4. Near-surface air temperatures simulated by the six numerical experiments (a–f, from EXP1 to EXP6, respectively) and observed measurements (g) at local noon on 12 March 2017, as well as spatial correlation coefficient (SCC) time series of near-surface air temperatures for the six experiments (X axis shows days in March; h). For a description of the experiments, see Table 2.

performance, that is, the highest RMSE, is obtained due to the simple albedo parametrization scheme used by the Noah LSM (Figure 5b).

3.3. Solid Precipitation

SD is an indicator of snow event intensity, but it does depend upon snow density. For example, dry snow is deeper than wet snow for a given SWE value. Generally speaking, SWE is an accurate descriptor of the actual

Table 5
SCC Between Observed Measurements of Near-Surface Air Temperatures and the Six Numerical Experiments; for a Description of the Experiments, See Table 2

EXP	SCC
EXP1	0.47
EXP2	0.46
EXP3	0.45
EXP4	0.41
EXP5	0.45
EXP6	0.44

Note. SCC = spatial correlation coefficient.

quantity of solid precipitation. We used observations of both SD and SWE to evaluate the model's performance in estimating solid precipitation values. The SD and SWE observations are obtained from CMA stations, and we focus on the solid precipitation records from 11 to 15 March 2017.

3.3.1. SD

We used SD observations from 122 in situ stations with observed SD records to evaluate the modeled estimates of SD. Because of the inhomogeneous distribution of these 122 stations across the TP, we partitioned the available observations into three regions according to their geographical locations (Figure 6a). Observations of snow traces, that is, where $SD \leq 0.1$, are coded by CMA as $SD = 999990.0$, but in our analyses we apply $SD = 0.1$ to evaluate the modeled estimates of snow traces. We find

that the number of SD observation records is the greatest at 08:00 BST, and we therefore select this observation time as the best at which to evaluate the model's performance.

The mean SD at 08:00 BST was calculated for each region (Figure 6b). It can be clearly seen that the most severe snowfall occurred in Region 3, with maximum SD reaching 50 cm, and the snow remaining deep thereafter. Maximum SD is less than 8 cm in the other two regions; the snow in Region 1 is about twice

as deep as that in Region 2. Region 1 experiences a maximum regional mean SD of 7.1 cm on 13 March, which thinned subsequently. Snow in Region 2 has a maximum regional mean SD of 3.2 cm on 12 March before decreasing.

The spatial distribution of SD observations and the estimates for all the experiments are shown in Figure 7. Deep snow (i.e., when $SD > 0.25$ m) on the southwestern TP, and shallow snow on the northeastern TP, is estimated for all six experiments, and appears consistent with observed SD values, apart from local deviations in some experiments. Snow cover data are retrieved from the Interactive Multisensor Snow and Ice Mapping System, which is a combination of various data sets acquired by optical and microwave sensors with in situ observations, to avoid any distortion from the cloud layer. It is documented that at the same time a large proportion of the TP is covered with snow, especially its northwestern area and the Himalaya Mountain region (Figure 7b). All experiments produce a similar spatial pattern of snow cover over the whole TP, though there is a considerable difference in SD range. Compared with the sparse meteorological station observations and the Ice Mapping System data, the model's appeared to be able to verify not only observed SD values at station surfaces but also the spatial distribution of snow cover rendered by the remote sensing product (Figure 7).

Differences in the model's performance across the six numerical experiments appear when close attention is paid to SD, particularly when the snow is deep. There are more ground observation stations on the eastern and central TP. SD values from these areas therefore form the basis of our analysis. It can be clearly seen that the WRF experiments using NCEP-FNL data sets (i.e., for EXP2, EXP4, and EXP6) give higher SD values than did the experiments using ERA-Interim data sets (i.e., for EXP1, EXP3, and EXP5), when the same LSM is applied. When applying the Noah LSM, that is, to EXP3 and EXP4, modeled estimates of snow coverage and deep snow extent are greater than those obtained when using WRF + CLM, that is, for EXP1 and EXP2, and WRF + Noah-MP, that is, for EXP5 and EXP6, and even from in situ records

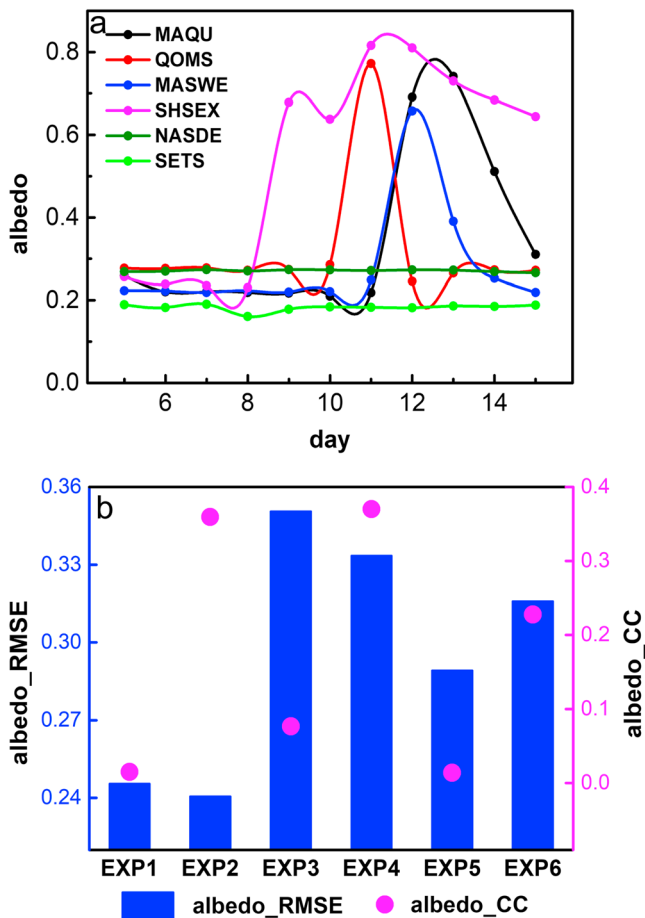


Figure 5. Daily observed albedo values at 14:00 BST (a; data points have been connected by applying splines; X axis shows days in March) and mean albedo root-mean-square error (RMSE) and correlation coefficient (CC) values (b; X axis shows the experiments listed in Table 2) at CAS stations during the snow event period. For a description of the CAS stations, see Table 4. CAS = Chinese Academy of Sciences.

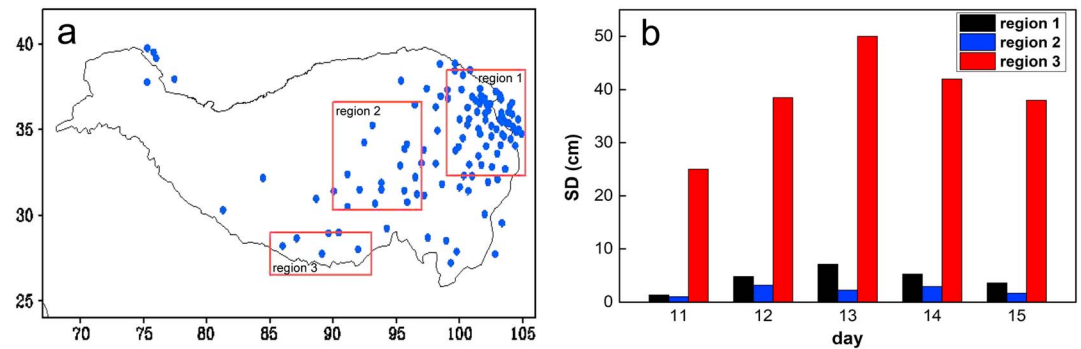


Figure 6. Distribution of China Meteorological Administration stations, with SD observations and partition of the snow depth into three regions (a); and time series of the mean SD values for each region observed at 08:00 BST from 11 to 15 March 2017 (b). SD = snow depth.

(Figure 7). Clearly, the modeled SD estimates are sensitive not only to the LSM used but also to initial and boundary conditions, at least for the severe snow event we analyze.

There are remarkable differences between the modeled SD and in situ ground observations. To understand better the causes of such inaccuracies in the model's SD estimates, we once again used mean SD values by region. The scatter and time series column of regional mean SD values are displayed in Figure 8. The observed mean SD value for Region 3 is higher than for Regions 1 and 2. The mean SD for Region 3 is observed to range between 25 cm and 50 cm, while the maximum mean SD estimate in the same region is only 10.1 cm for EXP1, 7.4 cm for EXP2, 19.1 cm for EXP3, 13.2 cm for EXP4, 11.3 cm for EXP5, and 8.1 cm for EXP6. The mean SD for Region 1 is observed to range between 1.4 cm and 7.1 cm. The mean SD estimate for Region 1 for EXP1 and EXP2 is about twice the corresponding observed value, except for a similar SD value on 12 March, while the mean SD estimate for the same region for EXP3 and EXP4 is more than twice the depth of that observed in situ; the maximum mean SD estimate is more than 20 cm for both EXP3 and EXP4. In Region 1, the minimum mean observed SD is 1.4 cm on 11 March, a value successfully simulated by EXP5. The maximum mean observed SD is 10.1 cm less than the mean modeled SD for EXP5, and 6.2 cm less than that modeled by EXP6. In Region 2, the mean observed SD ranges between 1.1 and 3.2 cm and is apparently overestimated by all six experiments, especially by EXP3 and EXP4, to which the Noah LSM is applied. Clearly, the model overestimates SD values for regions 1 and 2. A large underestimation of SD for Region 3 is evident, despite deep snow estimates (Figure 7). In Region 3, in situ SD measurements are sparse, and mismatches in the delineation of SD are apparent. Accordingly, we deem the evaluation of modeled SD estimates in this part of the TP unreliable. From 11 to 15 March, modeled SD estimates indicate ongoing snowfall in Region 1, with a reasonably constant SD in Region 2 (Figure 8). Moreover, modeled SD estimates using NCEP-FNL data or the Noah LSM for Region 1 suggest a time lag for snowfall and the subsequent snowmelt in comparison with actual observations (Figure 8b). Only EXP5 (using Noah-MP LSM + ERA-Interim) indicates snowfall in Region 2 (Figure 8c).

3.3.2. SWE

SWE is the product of snow density multiplied by SD, $\rho_{\text{snow}} \times \text{SD}$, and, therefore, is a better descriptor of the total quantity of solid precipitation than SD. We used SWE observations recorded at 20:00 BST from CMA stations on the TP and its surrounding regions to evaluate the model's SWE estimates. A large proportion of these meteorological stations are located on the eastern and central TP (i.e., 90°E eastwards), with no station in the Tibet Autonomous Region.

Observed and simulated results for SWE totals are displayed in Figure 9. We focus again on the snow event from 11 to 13 March 2017. Observed SWE measurements document significant solid precipitation near the northeastern fringe of the TP, with a maximum 3-day total SWE of 51.9 kg/m². The modeled results do not contradict these limited observations. The maximum total SWE values are estimated as being 57.5, 54.2, 58.4, 48.7, 45.9, and 42.3 kg/m² for EXP1 to EXP6 inclusive, respectively, for the eastern TP. Deviations between modeled and observed measurements are noticed in some instances, especially when greater SWE values are

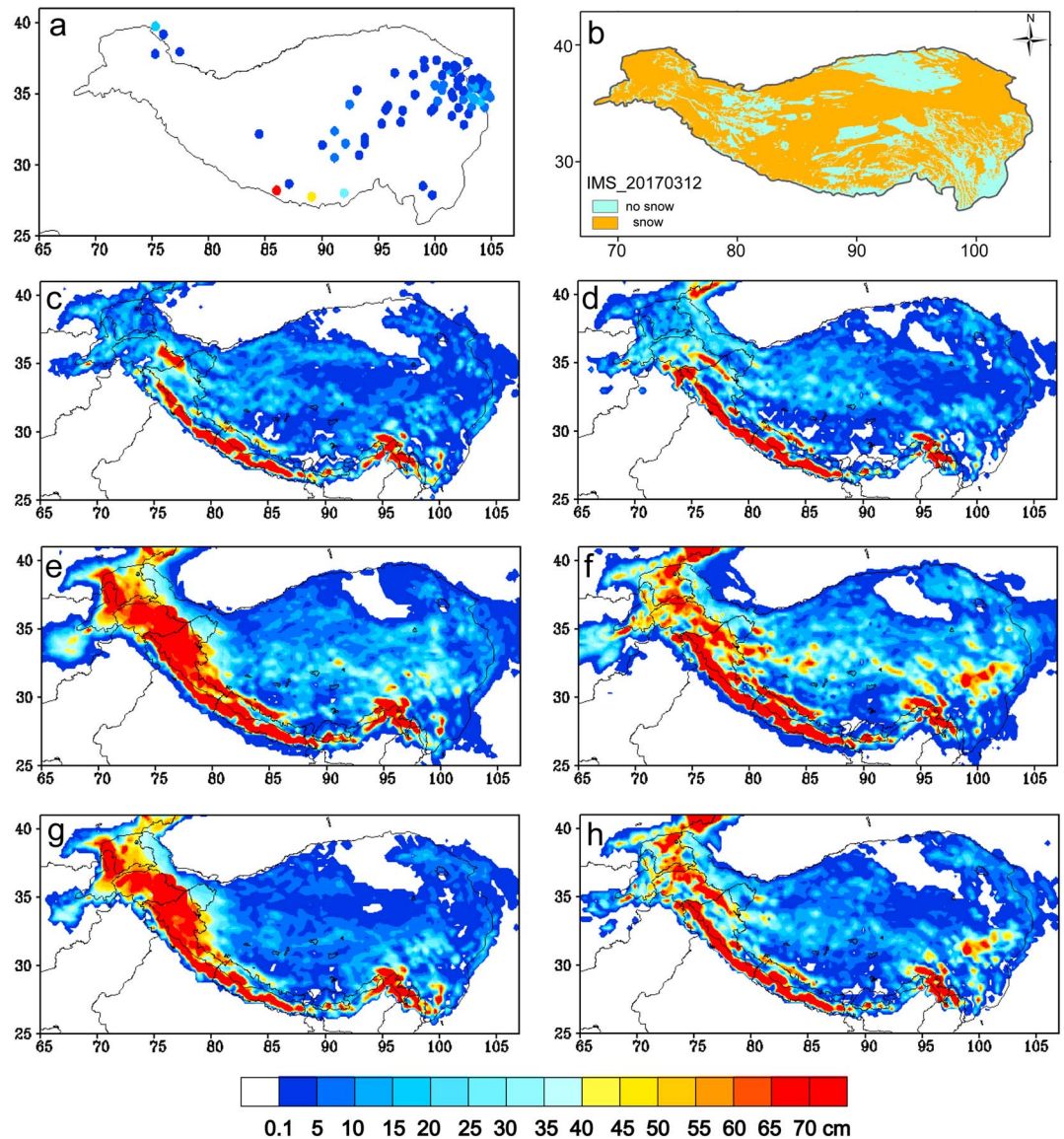


Figure 7. Snow depth observations from China Meteorological Administration meteorological stations (a), and estimates from the six numerical experiments (c–h; from EXP1 to EXP6, respectively), and the snow cover flag from the IMS program (b), all for 08:00 BST on 12 March 2017. For a description of the experiments, see Table 2.

involved. The modeled SWE values for the southeastern margins of the TP are higher than 133 kg/m^2 , whereas the observed values can be as low as 7 kg/m^2 . All experiments apparently overestimate the total solid precipitation on the southeastern TP, with a particularly wide range in significant SWE values (Figure 9). Snow densities can change in the course of snowfall and the subsequent evolution of the snowpack, especially when there is minimal fresh snow. All six experiments show low SWE values but high SD values in the northern Himalaya region when comparing Figure 9 with Figure 7, indicating fresh snowfalls in this region.

To rank the model's performance in the six numerical experiments more precisely, we used various skill scores such as the Threat Score (TS), the Equitable TS (ETS), the Efficient Hit (EH), the Not Hit (NH), the Point Over (PO), and the Bias analysis. SWE thresholds from 5 to 20 kg/m^2 were applied to calculate these skill scores. The TS and ETS values decrease with increasing SWE, especially when SWE is not less than 15 kg/m^2 , while NH and Bias increase with increasing SWE values (Figure 10). The ETS value is lower than the corresponding TS value for each threshold for every experiment. The ETS retains all the advantages of TS

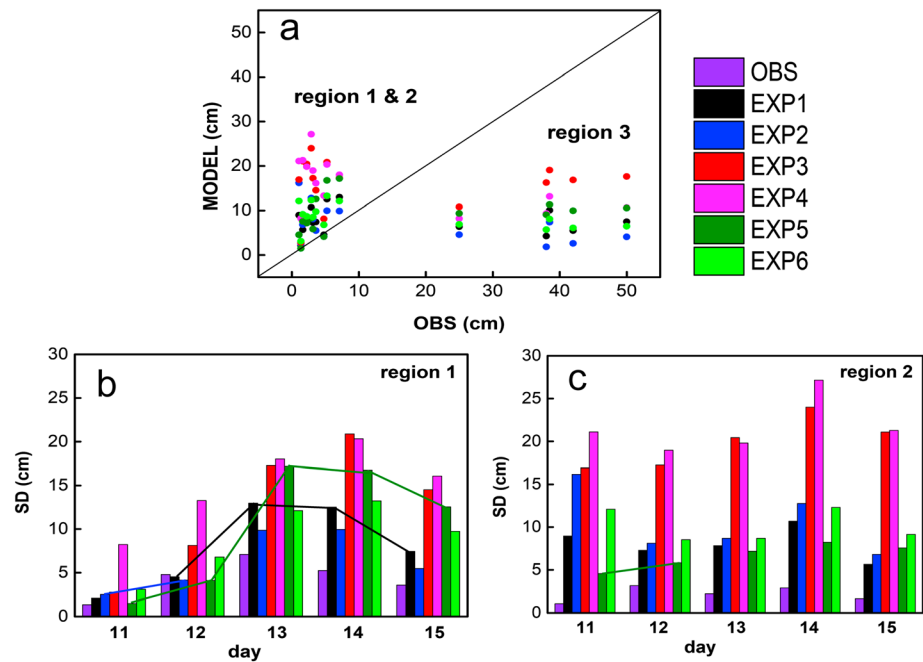


Figure 8. Scatterplot a and time series of mean observed and estimated SD values for Region 1 (b) and Region 2 (c; see Figure 8a) at 08:00 BST from 11 to 15 March 2017. For a description of the experiments, see Table 2.

and avoids the impact of random climate events. Looking at all six experiments together, the WRF model when applied using the Noah LSM gives higher TS and ETS values across the entire SWE range (Figures 10a and 10b), possibly due to the large range of modeled estimates of solid precipitation in EXP3 and EXP4. The PO score (not shown here) remains relatively low across the entire SWE range and is less than 0.4 when using a low SWE threshold (i.e., $SWE < 10 \text{ kg/m}^2$) while applying Noah LSM in the WRF model; this appears to demonstrate that WRF + Noah LSM has a certain capacity to model light snow, although instances with a larger bias do occur. NH and PO scores increase with increasing SWE, due to mismatches in the delineation of heavy snowfall (Figure 9). In these cases, many stations located on the southeastern TP do not report snow records, while modeled estimates suggest that no solid precipitation is present in the same region, leading most probably to very high EH values (i.e., $EH > 0.7$; not shown here). Overall, the WRF model exhibits an acceptable performance when estimating light snow, i.e., $SWE < 10 \text{ kg/m}^2$. When the WRF model is combined with CLM or the Noah-MP LSM, this is generally applicable to snow event simulations over the TP (Figure 10).

4. Discussion

Our experiments achieve a better performance when estimating albedo and near-surface air temperatures when applying CLM, confirming the results of Jin et al. (2010). This finding could potentially be explained by the advanced albedo parametrization scheme in CLM, which includes more albedo factors, that is, the solar zenith angle and effective ice grain size (Lawrence & Chase, 2010). Both wet and dry snow processes can drive rapid changes in albedo. Ice effective grain size is calculated by considering dry snow metamorphism, liquid water-induced metamorphism, liquid water refreezing and the addition of freshly fallen snow. The contribution of liquid water to enhanced metamorphism depends on the mass liquid water fraction, which is based on grain growth rates under different liquid water contents. The CLM's advanced albedo parametrization scheme could therefore have resulted in the more accurate calculation of albedo and net radiation, and thus the derived and diagnosed near-surface air temperatures in EXP1 and EXP2. It remains to be established whether further improvements in the parametrization of albedo would be both feasible and beneficial.

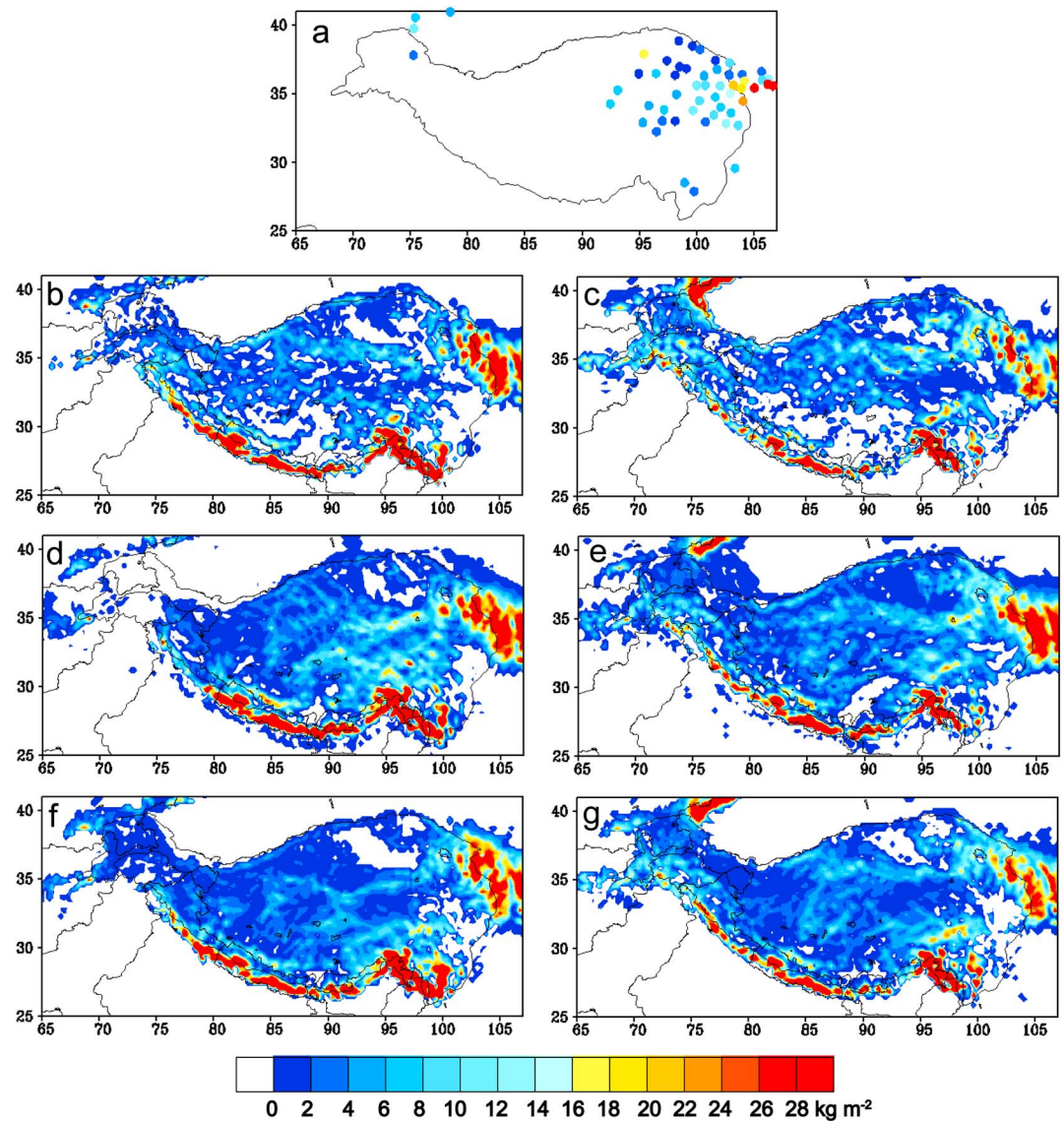


Figure 9. SWE observations (a) and SWE estimates from the six numerical experiments (b–g; from EXP1 to EXP6, respectively) for 11 to 13 March 2017. For a description of the experiments, see Table 2. SWE = snow water equivalent.

The model's performance in estimating near-surface air temperatures varies in response to the particular in situ locations of each of the meteorological stations and is therefore dependent upon the complexity of each station's local topography. A shady or sunny slope is defined by its aspect (i.e., the azimuthal direction of the surface), which in turn is determined by the topography of the surroundings. For example, a shady slope is taken as having a north-facing aspect between 0° and 45° , and 315° and 360° . A sunny slope has a south-facing aspect ranging between 135° and 225° . A detailed description of the model's performance depending in relation to aspect can be found in the supporting information.

In all six experiments high SD values are evident in the Himalaya region. This could be explained by the complex, high, mountainous terrain and low near-surface air temperatures. Remarkably low near-surface air temperatures are modeled at high altitudes in the Himalaya region. Ice crystals tend to form more frequently in the atmosphere and precipitate to the surface at high altitudes under low near-surface air temperature conditions. Thus, snowfall occurs frequently in the Himalaya Mountains. The lower near-surface air temperatures at high altitudes tend to reduce snowmelt rates, so that deeper snow is likely to occur under these conditions (Figure 7).

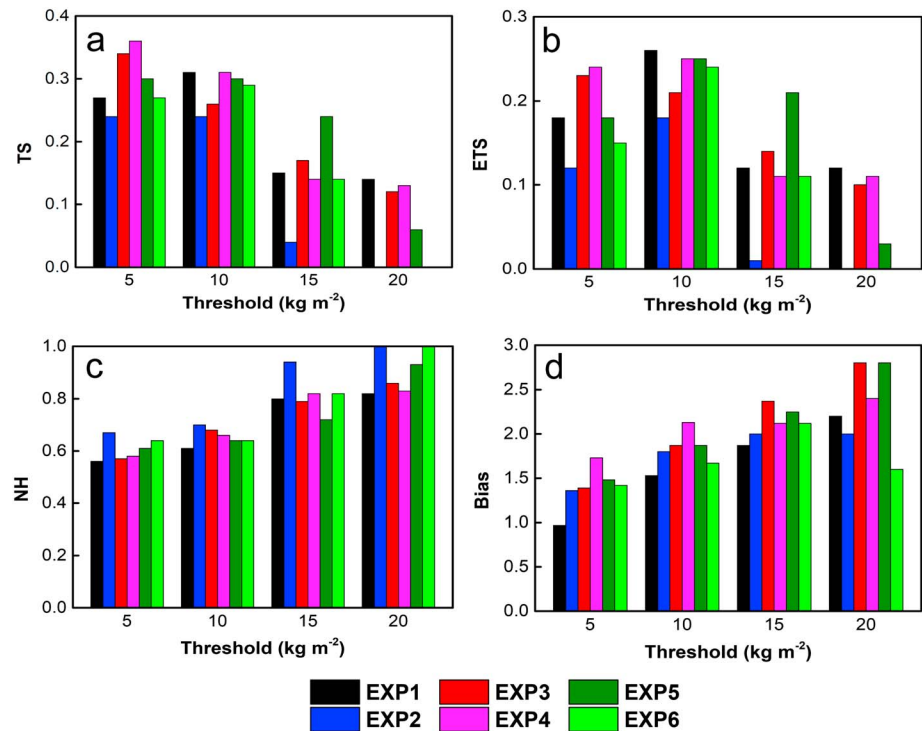


Figure 10. Threat Score (TS), Equitable TS (ETS), Not Hit (NH), and Bias SWE analyses by the six numerical experiments for 11 to 13 March 2017 (*X* axis shows SWE thresholds). For a description of the experiments, see Table 2. SWE = snow water equivalent.

All the experiments in our study greatly overestimate solid precipitation on the TP. This could have been because the simulation of solid precipitation over a complex terrain is known to respond most sensitively to cloud microphysics (Liu et al., 2011), because cloud microphysics affects the release of latent heat during the water vapor phase transition, thus impacting upon the drag of precipitation particles and the solid precipitation content. Yu's ensemble simulation results indicated that the Noah LSM and the Lin scheme performed better than other physics schemes, that is, WSM6, Thompson and RUC, in simulating snowfall over northeastern China (Yu, 2013). We therefore referred to Yu's ensemble simulations and applied a relatively sophisticated Lin microphysics scheme in our WRF modeling when simulating the specified snow event.

Six hydrometeors are included in the Lin microphysics scheme, that is, water vapor, cloud water, cloud ice, rain, snow, and graupel. The formation of solid precipitation is related to air temperature, particle concentration, particle radius, particle mass, and the terminal velocity of ice crystals. Yu (2013) demonstrated that the Lin microphysics scheme was applicable to snowfall events in northeastern China, but this does not immediately mean that it is equally applicable to the TP. Such an assumption may therefore provide one possible explanation for the model's SD overestimates is the use of constants to convert solid precipitation into SD. In the Lin scheme, snow is assumed to have a spherical shape with a constant bulk density of 100 kg/m³ (Lin et al., 1983). However, the snow density from pit observations in high, mountainous regions has been measured at 380 kg/m³ (Fujita et al., 1996) and 481 kg/m³ (Ayala et al., 2017). Applying such a higher snow density to the conversion of solid precipitation to SD would give a much lower modeled SD, that is, a value much closer to the observed SD. In spite of the shortcomings of the Lin scheme, our simulated results are still meaningful, because the study focuses solely on the sensitivity to LSMs and initial and boundary conditions.

Land surface type plays an important role in land-atmosphere interactions, and significantly affects the partitioning of surface energy fluxes (Crawford et al., 2001) and precipitation (Eltahir, 1998). Mismatches between the land surface types applied in the LSMs versus the actual land surface types is another

possible reason explaining the underestimation of near-surface air temperatures and the overestimation of solid precipitation, because radiation flux, near-surface air temperatures and the rate of snowmelt are affected by land surface type and fractional vegetation cover. In the future, we will attempt to apply real-time land cover and fractional vegetation cover data products into these severe snow event simulations in order to improve solid precipitation estimates. Additionally, further research will focus on the sensitivity of solid precipitation estimates to microphysics schemes over the complex topographies of the TP, as well as on adjusting the parameters of microphysical hydrometeor parametrization schemes in accordance with local observations in order to optimize ice nuclei activation scheme.

5. Summary and Conclusions

Frequent snowfall and snowmelt on the TP play important roles in the terrestrial water cycle (Nakajima, 2011). Such processes require an appropriate choice of not only parametrization schemes to describe land-atmosphere interactions but also atmospheric data sets to specify initial and boundary conditions. The purpose of our study is to understand the role of LSMs coupled with state-of-the-art WRF and then to find an optimal combination of LSMs (from the CLM, Noah, and Noah-MP protocols) and initial and boundary conditions provided by NCEP-FNL or ERA-Interim data sets to describe a severe snow event, which affected a large proportion of the TP. We chose a severe snow event, which occurred right across the TP in March 2017 and which exhibited a wide range of snowy conditions.

Snowfall and snowmelt depend on near-surface air temperatures, accompanied by drastic changes in albedo values. Our numerical experiments indicate that the temporal and spatial patterns in near-surface air temperatures are reasonably accurately reproduced. The sensitivity of near-surface air temperatures and albedo estimates to the applied LSMs is greater than to initial and boundary conditions. The albedo parametrization scheme in the CLM protocol performs better, since more albedo factors are taken into account, such as the solar zenith angle and effective ice grain size. WRF + CLM using ERA-Interim data performs best in near-surface air temperature estimates, with the smallest MAD (MAD = 7.3 °C) and RMSE (RMSE = 8.4 °C), and the highest CC (CC = 0.75) and SCC (~0.5). The coarse horizontal resolution configuration of the model and the mismatch in land surface types used in the model versus the actual land surface types are potential reasons for such large deviations. Both the Noah and Noah-MP LSMs give inferior estimates of near-surface air temperatures and albedo values, possibly due to their simpler albedo parametrization schemes, notwithstanding various complex physics schemes integrated into the Noah-MP LSM.

Our results document the impact of initial and boundary conditions on modeled estimates of SD. NCEP-FNL data set analyses produce much higher SD estimates than do ERA-Interim data set analyses for the eastern and central TP, with the reverse being the case in the Himalaya region. The sensitivity of SD estimates to the LSMs is further documented by higher estimates of SD and snow cover obtained using the Noah LSM compared to the other two LSMs. WRF modeling overestimates SD in Regions 1 and 2, while substantially underestimates SD in Region 3, possibly because of very few in situ SD observations and the large, terrain-related, spatial variability in SD values in Region 3. Further, SD estimates for the eastern TP suggest a time lag for snowfall and the subsequent snowmelt when NCEP-FNL data or the Noah LSM is applied. Only the Noah-MP + ERA-Interim elucidates a clear snowfall event on the central TP.

SWE is a better descriptor of the total quantity of solid precipitation. The spatial distribution of large SWE estimates is similar to the one obtained using in situ SWE observations, notwithstanding differences in the delineation of snow-covered areas. The maximum SWE observed on the eastern TP is 51.9 kg/m², an overestimate of <13% for EXP1, EXP2, and EXP3, but an underestimate of <19% for EXP4, EXP5, and EXP6. All six numerical experiments greatly overestimate total solid precipitation on the southeastern TP, at least in terms of SWE. Furthermore, the TS and ETS scores decrease with increasing SWE, while the NH and Bias values increase with increasing SWE. The numerical experiments which use a WRF + Noah LSM combination give higher TS and ETS scores, but a rather high Bias, possibly due to the wide range and high SWE values obtained in these experiments. Overall, the WRF model has capacity to estimate SWE where there is a low SWE threshold, that is, SWE <10 kg/m². The WRF + CLM or Noah-MP LSM configurations render the best estimates of SWE on the TP, at least for the snow event we analyze in this study.

This study demonstrates and evaluates the use of LSMs coupled with WRF modeling to describe a severe snow event that affected a large proportion of the TP. Our study may provide theoretical and empirical reference to researchers conducting numerical experiments on snow events in the same, or similar, complex, mountainous areas. Further attention needs to be paid to the role of LSMs in capturing land-atmosphere interactions. In our further investigations, we expect to focus on improving the WRF estimates of solid precipitation on the TP.

Acknowledgments

This research is supported by the Strategic Priority Research Program of Chinese Academy of Sciences, Grant XDA2006010103, the National Natural Science Foundation of China (91737205, 41661144043, 41830650, 91637313, and 91637312), the Key Research Program of Frontier Sciences of Chinese Academy of Sciences (QYZDJ-SSW-DQC019), and the SAFEA Long-Term Projects of the 1000 Talent Plan for High-Level Foreign Experts (Grant WQ20141100224). The authors express thanks to NCAR and ECMWF for sharing atmospheric reanalysis data sets (NCEP-FNL meteorological data is available from <https://rda.ucar.edu/datasets/ds083.3/>, and ERA-Interim data set is available from <http://apps.ecmwf.int/datasets/data/interim-full-daily/>), to National Snow and Ice Data Center (NSIDC) for providing remote sensing snow cover product (the product is available from <https://nsidc.org/data/g02156>), and to Linshan Liu from Institute of Geographic Sciences and Natural Resources Research, Chinese Academy of Sciences for sharing SRTM (the data set is available from <http://www.tpdatabase.cn/portal/index.jsp>), also to staff from CMA and CAS comprehensive observational stations (NASDE, SETS, QOMS, MASWE, SHSEX, and MAQU) for very hard work in meteorological observations over the Tibetan Plateau and offering the data. The authors are very grateful to the reviewers for their patience in reviewing the manuscript and offering abundant and constructive comments. The first author would like to express thanks to Liqiang Fan from CMA and acknowledge all group members especially Xuelong Chen, ChaoXu, and Binbin Wang for their help in completing this paper.

References

- Ayala, A., Pellicciotti, F., Peleg, N., & Burlando, P. (2017). Melt and surface sublimation across a glacier in a dry environment: Distributed energy-balance modelling of Juncal Norte Glacier, Chile. *Journal of Glaciology*, *63*(241), 803–822. <https://doi.org/10.1017/jog.2017.46>
- Berrisford, P., Dee, D. P., Poli, P., Brugge, R., Fielding, M., Fuentes, M., et al. (2009). The ERA-Interim archive, ERA report series, No. 1. ECMWF: Reading, UK.
- Blanford, H. F. (1884). On the connection of the Himalayan snowfall with dry winds and seasons of drought in India. *Proceedings of the Royal Society of London*, *37*, 3–22.
- Cai, X., Yang, Z. L., Xia, Y., Huang, M., Wei, H., Leung, L. R., & Ek, M. B. (2014). Assessment of simulated water balance from Noah, Noah-MP, CLM, and VIC over CONUS using the NLDAS test bed. *Journal of Geophysical Research: Atmospheres*, *119*, 13,751–13,770. <https://doi.org/10.1002/2014JD022113>
- Chen, F., Barlage, M., Tewari, M., Rasmussen, R., Jin, J., Lettenmaier, D., et al. (2014). Modeling seasonal snowpack evolution in the complex terrain and forested Colorado Headwaters region: A model intercomparison study. *Journal of Geophysical Research: Atmospheres*, *119*, 13,795–13,819. <https://doi.org/10.1002/2014JD022167>
- Chen, F., & Dudhia, J. (2001). Coupling an advanced land surface-hydrology model with the Penn State-NCAR MM5 modeling system. Part I: Model implementation and sensitivity. *Monthly Weather Review*, *129*(4), 569–585. [https://doi.org/10.1175/1520-0493\(2001\)129<0569:CAALSH>2.0.CO;2](https://doi.org/10.1175/1520-0493(2001)129<0569:CAALSH>2.0.CO;2)
- Chen, F., Liu, C., Dudhia, J., & Chen, M. (2014). A sensitivity study of high-resolution regional climate simulations to three land surface models over the western United States. *Journal of Geophysical Research: Atmospheres*, *119*, 7271–7291. <https://doi.org/10.1002/2014JD021827>
- Collier, E., Molg, T., Maussion, F., Scherer, D., Mayer, C., & Bush, A. B. G. (2013). High-resolution interactive modelling of the mountain glacier-atmosphere interface: An application over the Karakoram. *The Cryosphere*, *7*(3), 779–795. <https://doi.org/10.5194/tc-7-779-2013>
- Crawford, T. M., Stensrud, D. J., Mora, F., Merchant, J. W., & Wetzel, P. J. (2001). Value of incorporating satellite-derived land cover data in MM5/PLACE for simulating surface temperatures. *Journal of Hydrometeorology*, *2*(5), 453–468. [https://doi.org/10.1175/1525-7541\(2001\)002<0453:VOISDL>2.0.CO;2](https://doi.org/10.1175/1525-7541(2001)002<0453:VOISDL>2.0.CO;2)
- Dee, D. P., Uppala, S. M., Simmons, A. J., Berrisford, P., Poli, P., Kobayashi, S., et al. (2011). The ERA-Interim reanalysis: Configuration and performance of the data assimilation system. *Quarterly Journal of the Royal Meteorological Society*, *137*(656), 553–597. <https://doi.org/10.1002/qj.828>
- Dodson, R., & Marks, D. (1997). Daily air temperature interpolated at high spatial resolution over a large mountainous region. *Climate Research*, *8*(1), 1–20.
- Eltahir, E. A. B. (1998). A soil moisture rainfall feedback mechanism. 1. Theory and Observations. *Water Resources Research*, *34*, 765–776.
- Fujita, K., Seko, K., Ageta, Y., Jianchen, P., & Tandong, Y. (1996). Superimposed ice in glacier mass balance on the Tibetan Plateau. *Journal of Glaciology*, *42*(142), 454–460. <https://doi.org/10.1017/S0022143000003440>
- Gao, L., Bernhardt, M., Schulz, K., & Chen, X. W. (2017). Elevation correction of ERA-interim temperature data in the Tibetan Plateau. *International Journal of Climatology*, *37*(9), 3540–3552. <https://doi.org/10.1002/joc.4935>
- Gao, X. J., Zhao, Z. C., & Giorgi, F. (2002). Changes of extreme events in regional climate simulations over East Asia. *Advances in Atmospheric Sciences*, *19*(5), 927–942.
- Gao, Y. H., Xu, J. W., & Chen, D. L. (2015). Evaluation of WRF Mesoscale Climate Simulations over the Tibetan Plateau during 1979–2011. *Journal of Climate*, *28*(7), 2823–2841. <https://doi.org/10.1175/JCLI-D-14-00300.1>
- Gerlitz, L., Conrad, O., Thomas, A., & Bohner, J. (2014). Warming patterns over the Tibetan Plateau and adjacent lowlands derived from elevation- and bias-corrected ERA-Interim data. *Climate Research*, *58*(3), 235–246. <https://doi.org/10.3354/cr01193>
- Giorgi, F., Coppola, E., Solmon, F., Mariotti, L., Sylla, M. B., Bi, X., et al. (2012). RegCM4: Model description and preliminary tests over multiple CORDEX domains. *Climate Research*, *52*, 7–29. <https://doi.org/10.3354/cr01018>
- Grotjahn, R. (2008). Different data, different general circulations? A comparison of selected fields in NCEP/DOE AMIP-II and ECMWF ERA-40 reanalyses. *Dynamics of Atmospheres and Oceans*, *44*(3–4), 108–142. <https://doi.org/10.1016/j.dynatmoce.2007.08.001>
- Ikedo, K., Rasmussen, R., Liu, C., Gochis, D., Yates, D., Chen, F., et al. (2010). Simulation of seasonal snowfall over Colorado. *Atmospheric Research*, *97*(4), 462–477. <https://doi.org/10.1016/j.atmosres.2010.04.010>
- Ji, Z. M., & Kang, S. C. (2013). Projection of snow cover changes over China under RCP scenarios. *Climate Dynamics*, *41*(3–4), 589–600. <https://doi.org/10.1007/s00382-012-1473-2>
- Jin, J. M., Miller, N. L., & Schlegel, N. (2010). Sensitivity study of four land surface schemes in the WRF mode. *Advances in Meteorology*, *2010*, 167436. <https://doi.org/10.1155/2010/167436>
- Kalinin, N. A., Shikhov, A. N., & Sviyazov, E. M. (2015). Simulation of snow accumulation and melt in the Votkinsk reservoir catchment using the WRF-ARW model. *Russian Meteorology and Hydrology*, *40*(11), 749–757. <https://doi.org/10.3103/S1068373915110059>
- Kalnay, E., Kanamitsu, M., Kistler, R., Collins, W., Deaven, D., Gandin, L., et al. (1996). The NCEP/NCAR 40-year reanalysis project. *Bulletin of the American Meteorological Society*, *77*(3), 437–471. [https://doi.org/10.1175/1520-0477\(1996\)077<0437:TNYP>2.0.CO;2](https://doi.org/10.1175/1520-0477(1996)077<0437:TNYP>2.0.CO;2)
- Kryza, M., Walaszek, K., Ojrzynska, H., Szymanowski, M., Werner, M., & Dore, A. J. (2017). High-resolution dynamical downscaling of ERA-Interim using the WRF regional climate model for the area of Poland. Part 1: Model configuration and statistical evaluation for the 1981–2010 period. *Pure and Applied Geophysics*, *174*(2), 511–526. <https://doi.org/10.1007/s00024-016-1272-5>
- Kunkel, K. E. (1989). Simple procedures for extrapolation of humidity variables in the mountainous Western United States. *Journal of Climate*, *2*(7), 656–670. [https://doi.org/10.1175/1520-0442\(1989\)002<0656:SPFEOH>2.0.CO;2](https://doi.org/10.1175/1520-0442(1989)002<0656:SPFEOH>2.0.CO;2)

- Lawrence, P. J., & Chase, T. N. (2010). Investigating the climate impacts of global land cover change in the community climate system model. *International Journal of Climatology*, *30*(13), 2066–2087. <https://doi.org/10.1002/joc.2061>
- Li, M., Ma, Y., Hu, Z., Ishikawa, H., & Oku, Y. (2009). Snow distribution over the Namco lake area of the Tibetan Plateau. *Hydrology and Earth System Sciences*, *13*(11), 2023–2030. <https://doi.org/10.5194/hess-13-2023-2009>
- Lin, Y. L., Farley, R. D., & Orville, H. D. (1983). Bulk parameterization of the snow field in a cloud model. *Journal of Climate and Applied Meteorology*, *22*(6), 1065–1092. [https://doi.org/10.1175/1520-0450\(1983\)022<1065:BPOTSF>2.0.CO;2](https://doi.org/10.1175/1520-0450(1983)022<1065:BPOTSF>2.0.CO;2)
- Liston, G. E., & Elder, K. (2006). A meteorological distribution system for high-resolution terrestrial modeling (MicroMet). *Journal of Hydrometeorology*, *7*(2), 217–234. <https://doi.org/10.1175/JHM486.1>
- Liu, C. H., Ikeda, K., Thompson, G., Rasmussen, R., & Dudhia, J. (2011). High-resolution simulations of wintertime precipitation in the Colorado headwaters region: Sensitivity to physics parameterizations. *Monthly Weather Review*, *139*(11), 3533–3553. <https://doi.org/10.1175/Mwr-D-11-00009.1>
- Liu, J., & Chen, R. (2011). Studying the spatiotemporal variation of snow-covered days over China based on combined use of MODIS snow-covered days and in-situ observations. *Theoretical and Applied Climatology*, *106*(3–4), 355–363. <https://doi.org/10.1007/s00704-011-0441-9>
- Liu, Y., & Qian, Z. (2005). *The affection of land and sea thermal difference to climate change in China* (pp. 1–193). Beijing: China Meteorological Press.
- Ma, W. Q., & Ma, Y. M. (2016). Modeling the influence of land surface flux on the regional climate of the Tibetan Plateau. *Theoretical and Applied Climatology*, *125*(1–2), 45–52. <https://doi.org/10.1007/s00704-015-1495-x>
- Ma, Y. M., Kang, S., Zhu, L., Xu, B., Tian, L., & Yao, T. (2008). Tibetan observation and research platform atmosphere-land interaction over a heterogeneous landscape. *Bulletin of the American Meteorological Society*, *89*(10), 1487–1492.
- Mausson, F., Scherer, D., Finkelnburg, R., Richters, J., Yang, W., & Yao, T. (2011). WRF simulation of a precipitation event over the Tibetan Plateau, China—An assessment using remote sensing and ground observations. *Hydrology and Earth System Sciences*, *15*(6), 1795–1817. <https://doi.org/10.5194/hess-15-1795-2011>
- Mausson, F., Scherer, D., Molg, T., Collier, E., Curio, J., & Finkelnburg, R. (2014). Precipitation seasonality and variability over the Tibetan Plateau as resolved by the high Asia reanalysis. *Journal of Climate*, *27*(5), 1910–1927. <https://doi.org/10.1175/Jcli-D-13-00282.1>
- Nakajima, C. (2011). Tibetan plateau as the water resource of Asia. *Journal of Geography*, *98*, 587–599.
- Niu, G. Y., Yang, Z. L., Mitchell, K. E., Chen, F., Ek, M. B., Barlage, M., et al. (2011). The community Noah land surface model with multiparameterization options (Noah-MP): 1. Model description and evaluation with local-scale measurements. *Journal of Geophysical Research*, *116*, D121109. <https://doi.org/10.1029/2010JD015139>
- Pleim, J. E., & Xiu, A. (1995). Development and testing of a surface flux and planetary boundary-layer model for application in mesoscale models. *Journal of Applied Meteorology*, *34*(1), 16–32. <https://doi.org/10.1175/1520-0450-34.1.16>
- Qin, D. H., Liu, S. Y., & Li, P. J. (2006). Snow cover distribution, variability, and response to climate change in Western China. *Journal of Climate*, *19*, 1820–1833.
- Qiu, J. (2008). The third pole. *Nature*, *454*(7203), 393–396. <https://doi.org/10.1038/454393a>
- Renwick, J. A. (2004). Trends in the Southern Hemisphere polar vortex in NCEP and ECMWF reanalyses. *Geophysical Research Letters*, *31*, L07209. <https://doi.org/10.1029/2003GL019302>
- Roesch, A., Wild, M., Gilgen, H., & Ohmura, A. (2001). A new snow cover fraction parametrization for the ECHAM4 GCM. *Climate Dynamics*, *17*(12), 933–946. <https://doi.org/10.1007/s003820100153>
- Russell, S. V., & Cai, M. (2004). Impact of land-use change on climate. *Nature*, *427*(6971), 213–214.
- Sato, T., Yoshikane, T., Satoh, M., Miltra, H., & Fujinami, H. (2008). Resolution dependency of the diurnal cycle of convective clouds over the Tibetan Plateau in a mesoscale model. *Journal of the Meteorological Society of Japan*, *86a*, 17–31. <https://doi.org/10.2151/jmsj.86a.17>
- Skamarock, W., Klemp, J. B., Dudhia, J., Gill, D. O., Barker, D. M., Wang, W., & Powers, J. G. (2008). A description of the advanced research WRF version 3, NCAR Technical Note NCAR/TN-475+STR.
- Smirnova, T. G., Brown, J. M., Benjamin, S. G., & Kim, D. (2000). Parameterization of cold-season processes in the MAPS land-surface scheme. *Journal of Geophysical Research*, *105*(D3), 4077–4086. <https://doi.org/10.1029/1999JD901047>
- Soares, P. M. M., Cardoso, R. M., Miranda, P. M. A., de Medeiros, J., Belo-Pereira, M., & Espirito-Santo, F. (2012). WRF high resolution dynamical downscaling of ERA-Interim for Portugal. *Climate Dynamics*, *39*(9–10), 2497–2522. <https://doi.org/10.1007/s00382-012-1315-2>
- Stahl, K., Moore, R. D., Floyer, J. A., Asplin, M. G., & McKendry, I. G. (2006). Comparison of approaches for spatial interpolation of daily air temperature in a large region with complex topography and highly variable station density. *Agricultural and Forest Meteorology*, *139*(3–4), 224–236. <https://doi.org/10.1016/j.agrformet.2006.07.004>
- Toure, A. M., Rodell, M., Yang, Z. L., Beaudoin, H., Kim, E., Zhang, Y., & Kwon, Y. (2016). Evaluation of the snow simulations from the community land model, version 4 (CLM4). *Journal of Hydrometeorology*, *17*(1), 153–170. <https://doi.org/10.1175/Jhm-D-14-0165.1>
- Wei, Z. G., & Dong, W. J. (2015). Assessment of simulations of snow depth in the Qinghai-Tibetan Plateau using CMIP5 multi-models. *Arctic, Antarctic, and Alpine Research*, *47*(4), 611–625. <https://doi.org/10.1657/Aaar0014-050>
- Xia, K., Wang, B., Li, L. J., Shen, S., Huang, W. Y., Xu, S. M., et al. (2014). Evaluation of snow depth and snow cover fraction simulated by two versions of the flexible global ocean-atmosphere-land system model. *Advances in Atmospheric Sciences*, *31*(2), 407–420. <https://doi.org/10.1007/s00376-013-3026-y>
- Xiao, Z. X., & Duan, A. M. (2016). Impacts of Tibetan Plateau snow cover on the interannual variability of the East Asian summer monsoon. *Journal of Climate*, *29*(23), 8495–8514. <https://doi.org/10.1175/JCLI-D-16-0029.1>
- Xie, Z. P., Hu, Z., Xie, Z., Jia, B., Sun, G., Du, Y., & Song, H. (2018). Impact of the snow cover scheme on snow distribution and energy budget modeling over the Tibetan Plateau. *Theoretical and Applied Climatology*, *131*(3–4), 951–965. <https://doi.org/10.1007/s00704-016-2020-6>
- Xue, Y., Sellers, P. J., Kinter, J. L., & Shukla, J. (1991). A simplified biosphere model for global climate studies. *Journal of Climate*, *4*(3), 345–364. [https://doi.org/10.1175/1520-0442\(1991\)004<0345:ASBMFG>2.0.CO;2](https://doi.org/10.1175/1520-0442(1991)004<0345:ASBMFG>2.0.CO;2)
- Yang, Z. L., Niu, G. Y., Mitchell, K. E., Chen, F., Ek, M. B., Barlage, M., et al. (2011). The community Noah land surface model with multiparameterization options (Noah-MP): 2. Evaluation over global river basins. *Journal of Geophysical Research*, *116*, D12110. <https://doi.org/10.1029/2010JD015140>
- Yu, E. T. (2013). High-resolution seasonal snowfall simulation over Northeast China. *Chinese Science Bulletin*, *58*(12), 1412–1419. <https://doi.org/10.1007/s11434-012-5561-9>
- Zhang, J. Y., Wang, W. C., & Wei, J. F. (2008). Assessing land-atmosphere coupling using soil moisture from the Global Land Data Assimilation System and observational precipitation. *Journal of Geophysical Research*, *113*, D17119. <https://doi.org/10.1029/2008JD009807>

- Zhang, Y., Li, T., & Wang, B. (2004). Decadal change of the spring snow depth over the Tibetan Plateau: The associated circulation and influence on the East Asian summer monsoon. *Journal of Climate*, *17*(14), 2780–2793. [https://doi.org/10.1175/1520-0442\(2004\)017<2780:DCOTSS>2.0.CO;2](https://doi.org/10.1175/1520-0442(2004)017<2780:DCOTSS>2.0.CO;2)
- Zhao, P., Zhou, Z., & Liu, J. (2007). Variability of Tibetan spring snow and its associations with the hemispheric extratropical circulation and East Asian summer monsoon rainfall: An observational investigation. *Journal of Climate*, *20*(15), 3942–3955. <https://doi.org/10.1175/JCLI4205.1>
- Zhu, X., & Dong, W. J. (2013). Evaluation and projection of northern hemisphere March–April snow covered area simulated by CMIP5 coupled climate models. *Advances in Climate Change Research*, *9*(3), 173–234. <https://doi.org/10.3969/j.issn.1673-1719.2013.03.003>